IEEE Photonics Journal
An IEEE Photonics Society Publication

Polarization-Independent Mode-Evolution-Based Coupler for the Silicon-on-Insulator Platform

Volume 10, Number 3, June 2018

Yun Wang
Luhua Xu
Han Yun
Minglei Ma
Amar Kumar
Eslam El-Fiky
Rui Li
Nicolás Abadíacalvo
Lukas Chrostowski
Nicolas A. F. Jaeger
David V. Plant

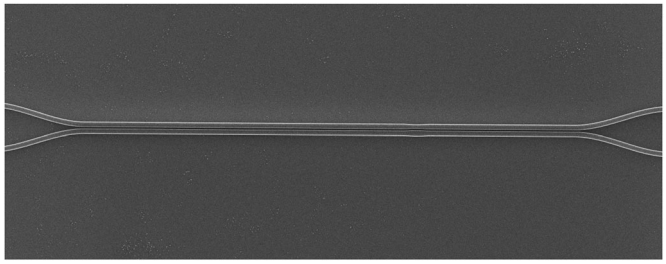

DOI: 10.1109/JPHOT.2018.2835767
1943-0655 © 2018 IEEE

IEEE photonics SOCIETY

IEEE

Polarization-Independent Mode-Evolution-Based Coupler for the Silicon-on-Insulator Platform

Yun Wang,[1] **Luhua Xu**,[1] **Han Yun**,[2] **Minglei Ma**,[2] **Amar Kumar**,[1] **Eslam El-Fiky**,[1] **Rui Li**,[1] **Nicolás Abadíacalvo**,[1] **Lukas Chrostowski**,[2] **Nicolas A. F. Jaeger**,[2] **and David V. Plant**[1]

[1]Department of Electrical and Computer Engineering, McGill University, Montreal, QC H3A 0G4, Canada
[2]Department of Electrical and Computer Engineering, University of British Columbia, Vancouver, BC V6T 1Z4, Canada

DOI:10.1109/JPHOT.2018.2835767

Manuscript received March 9, 2018; revised April 20, 2018; accepted May 9, 2018. Date of publication May 14, 2018; date of current version June 7, 2018. Natural Sciences and Engineering Research Council (NSERC) provided the financial support for the research. Corresponding author: Yun Wang (e-mail: yun.wang5@mcgill.ca).

Abstract: We demonstrate a polarization-independent mode-evolution-based coupler for the silicon-on-insulator platform. The measured coupler has negligible insertion loss over a bandwidth of about 100 nm, i.e., from 1500 to 1600 nm. The measured maximum power imbalances for the polarization-independent coupler are 1.2 and 0.2 dB for the fundamental transverse electric (TE_{00}) mode and the fundamental transverse magnetic (TM_{00}) mode, respectively. Our coupler also has a compact design footprint with mode-evolution region not more than 75$-\mu$m long.

Index Terms: Silicon nanophotonics, waveguide devices.

1. Introduction

The silicon-on-insulator (SOI) platform has opened the door for designers to make highly integrated photonic circuits. With the recent growth in silicon photonics technology, we have seen a transition from electrical interconnects to optical interconnects. Optical couplers are essential components in photonic integrated circuits (PICs), and 2 $\times$ 2 couplers are among the most fundamental components and are often used in transceivers [1], [2], switches [3], [4], etc. Mode-evolution-based couplers [5]–[10], multimode interference (MMI) couplers [11], [12], and conventional directional couplers (DCs) [13]–[15] are the three most commonly used optical couplers for the SOI platform. The operating principles of the MMI couplers and the conventional DCs involve the interference of multiple modes and, therefore, the performance of such devices relies on precise control of the device dimensions. In contrast, the main operating principle of the mode-evolution-based couplers involves the evolution of individual modes and, therefore, the performance of such devices is not sensitive to variations in device dimensions. In general, mode-evolutions-based couplers have broad operating bandwidths and high fabrication tolerances, which are their major advantages. In addition to being used as optical couplers, mode-evolution-based devices have been used to make polarization splitters [16], polarization rotators [17], and polarization rotator-splitters [18]. The

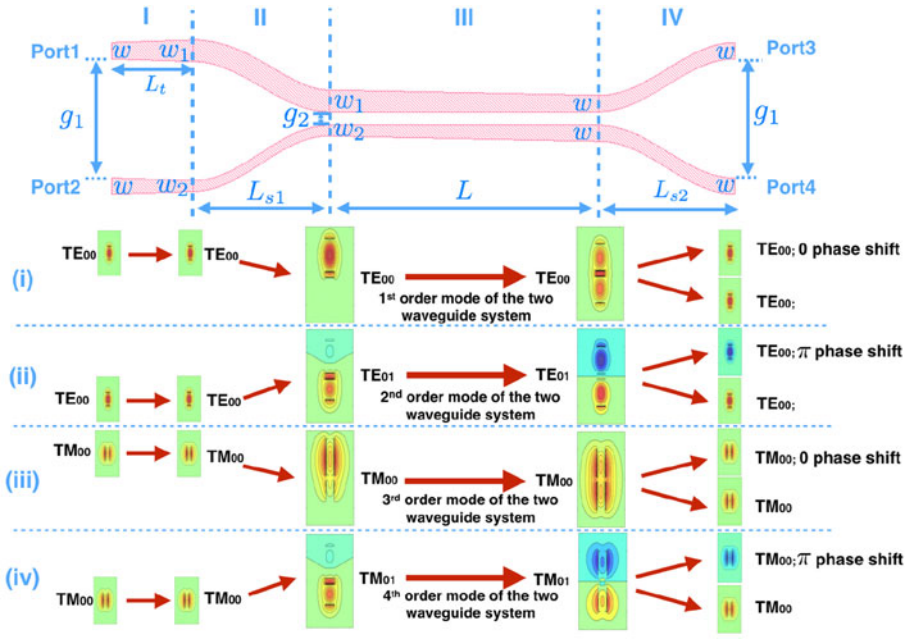

Fig. 1. A general schematic for a mode-evolution-based coupler with labelled design parameters and illustrations of the mode profiles at particular locations in the device; evolution of the (i) 1st order mode, (ii) 2nd order mode, (iii) 3rd order mode, and (iv) 4th order mode.

drawback of mode-evolutions-based devices is that, in order to avoid the excitation of unwanted modes, smooth transitions in geometry are required, which often results in long devices. Various mode-evolution-based couplers have been reported for the SOI platform, including rib waveguide based couplers [6], [10], strip waveguide based couplers [5], [7], and sub-wavelength grating based couplers [9]. In principle, mode-evolution-based couplers can be both wavelength and polarization independent [19]. However, the mode-evolution-based couplers that have been demonstrated so far are only designed for a single polarization, i.e., either for the fundamental transverse electric (TE_{00}) mode or for the fundamental magnetic (TM_{00}) mode.

In this paper, we demonstrate a polarization independent mode-evolution based coupler for the silicon-on-insualtor (SOI) platform. A segmented design approach, based on a combination of the 3D finite-difference time-domain (FDTD) and eigenmode expansion (EME) methods, will be presented to optimize the various design parameters of our coupler, which dramatically improved the design efficiency of such devices. As compared to the existing designs [5]–[10], our coupler has smaller design footprint, with a mode-evolution region of 75 μm. Our couplers are designed for SOI wafers with a 220 nm silicon layer, which are used by many Multi Project Wafer (MPW) foundries [20].

2. Design and Simulation

A general schematic for our coupler, which consists of four regions, is shown in Fig. 1. In Region I, two parallel waveguides, with widths of w and separated by a gap of g_1, are linearly tapered to have widths of w_1 and w_2. In Region II, using two S-bend waveguides of widths w_1 and w_2, the dissimilar waveguides are brought together until they are separated by a gap of g_2. Region III is the mode evolution region and has a length L. In Region III, the two waveguides with widths w_1 and w_2 are linearly tapered until both have widths of w, while maintaining a constant g_2. In Region IV, the two waveguides of width w are decoupled using two S-bend waveguides.

2.1 Operating Principle

The operating principle of each of our coupler can be explained as follows. On the left-hand side of Region I, the two waveguides of width w, separated by a gap of g_1, are far enough apart that coupling between them is negligible. On the right-hand side of Region I, the two waveguides have been linearly tapered to have widths that will ensure that when they are brought close together, i.e., separated by a gap of g_2, the coupling between them will remain negligible. In Region II, S-bend waveguides are used to bring the dissimilar waveguides together from a gap of g_1 to a gap of g_2. Depending on the injected mode type, i.e., TE_{00} or TM_{00}, and the input port, i.e., Port1 or Port2, an individual mode of the two waveguide system will be excited on the left-hand side of Region III and propagate throughout Region III without coupling to any other modes. In what follows, we will order the modes of the two waveguide system based on the magnitudes of their effective indices. The mode with the highest effective index becomes the 1st order mode and the mode with the second highest effective index becomes the 2nd order mode and so on. When the TE_{00} mode is injected into Port1, only the 1st order mode of the two waveguide system will be excited and preserved throughout Region III. The mode is mainly contained in the wider waveguide on the left-hand side of Region III and evolves to be symmetrically distributed across both waveguides on the right-hand side of Region III, as shown in Fig. 1(i). When the TE_{00} mode is injected into Port2, only the 2nd order mode of the two waveguide system will be excited and preserved throughout Region III. The mode is mainly contained in the narrower waveguide on the left-hand side of Region III and evolves to be anti-symmetrically distributed across both waveguides on the right-hand side of Region III, as shown in Fig. 1(ii). When the TM_{00} mode is injected into Port1, only the 3rd order mode of the two waveguide system will be excited and preserved throughout Region III. The mode is mainly contained in the wider waveguide on the left-hand side of Region III and evolves to be symmetrically distributed across both waveguides on the right-hand side of Region III, as shown in Fig. 1(iii). When the TM_{00} mode is injected into Port2, only the 4th order mode of the two waveguide system will be excited and preserved throughout Region III. The mode is mainly contained in the narrower waveguide on the left-hand side of Region III and evolves to be anti-symmetrically distributed across both waveguides on the right-hand side of Region III, as shown in Fig. 1(iv). When the TE_{00} mode is injected into either Port3 or Port4, the 1st order mode and the 2nd order mode of the two waveguide system will be excited on the right-hand side of Region III and evolve into the 1st order mode and the 2nd order mode on the left-hand side of Region III and couple to the TE_{00} modes of Port1 and Port2, respectively. Alternatively, when the TM_{00} mode is injected into either Port3 or Port4, the 3rd order mode and the 4th order mode will be excited on the right-hand side of Region III and evolve into the 3rd order mode and the 4th order mode on the left-hand side of Region III and couple to the TM_{00} modes of Port1 and Port2, respectively. It should be noted that when either mode type, i.e., TE_{00} or TM_{00}, is injected into Port1, the excited mode in Region III is a symmetric mode and, ideally, the field distributions have 0 relative phase shift at Port3 and Port4. In contrast, when either mode type, i.e., TE_{00} or TM_{00}, is injected into Port2, the excited mode in Region III is an anti-symmetric mode and, ideally, the field distributions have a π relative phase shift at Port3 and Port4.

2.2 Design Parameter Optimization

The most important characteristics of a mode-evolution-based coupler are the insertion loss (IL) and the power imbalance. Additionally, the operating bandwidth, fabrication tolerance, and space efficiency have become increasingly important, especially when used in PICs. Due to the large number of design parameters and the large footprint, it is computationally intensive and time-consuming to optimize a mode-evolution-based coupler using a brute-force optimization method for the entire structure. We use a segmented optimization approach, which optimizes our coupler in each of the four regions shown in Fig. 1. The values of w and g_2 of our couplers are decided upon before the optimization process. The value used for w is 450 nm, which provides single mode operation of a waveguide formed in an SOI platform with a 220 nm-thick silicon layer and a 2 μm-thick

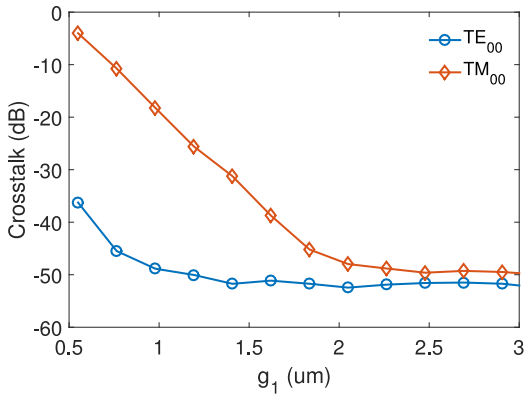

Fig. 2. Simulated crosstalk as a functions of g_1 between two, 10 μm-long, waveguides, each with width 450 nm.

silicon dioxide cladding layer [21]. In general, the smaller that g_2 is, the shorter the mode-evolution region can be; therefore, a small g_2 is preferred. In reality, g_2 is limited by the minimum feature size of the fabrication process. Though here we use electron beam lithography for the fabrication of our devices, which has a minimum feature size of about 50 nm, we choose g_2 to be 100 nm so that our designs will be compatible with advanced CMOS fabrication technologies [22].

In the first step of our design process, we use 3D FDTD simulations to determine g_1 of our coupler. The value of g_1 is determined based on the crosstalk between two parallel, 10 μm-long, waveguides each with width 450 nm, i.e., having the same width as those that will be connected to our devices on the left-hand side of Region I. The simulated crosstalk between the two waveguides as functions of g_1, for the TE_{00} and the TM_{00} modes are shown in Fig. 2. The crosstalk for the TE_{00} mode is smaller than that for the TM_{00} mode due to the higher mode confinement. Based on the simulation results shown in Fig. 2, we can see that the crosstalk saturate at 1.5 μm and 2.5 μm for the TE_{00} and the TM_{00} modes, respectively. These values also agree with the recommended waveguide spacings for routing waveguides in PICs [21]. Therefore, we choose $g_1 = 2.5\,\mu$m for our to accommodate both polarizations.

In the second step, we use 3D FDTD simulations to determine w_1, w_2, and L_{s1}. A waveguide width difference, $\delta w = w_1 - w_2$, is introduced to ensure that the coupling between the two waveguides and excitation of unwanted modes are negligible when they are brought together on the right-hand side of Region II. We inject the input modes into the top or bottom S-bend waveguide from the left-hand side of Region II and use mode expansion monitors on the right-hand side of Region II to calculate the ILs of the input mode, which includes both the bending loss and the loss caused by the excitation of unwanted modes. For example, when the TE_{00} mode is injected into the top waveguide from the left-hand side of Region II, the IL of the S-bend is equal to the ratio of the power injected in the TE_{00} mode and the power measured in the 1st order mode of the two waveguide system on the right-hand side of Region II. As another example, when the TM_{00} mode is injected into the bottom waveguide from the left-hand side of Region II, the IL of the S-bend is equal to the ratio of the power injected in the TM_{00} mode and the power measured in the 4th order mode of the two waveguide system on the right-hand side of Region II. As we increase δw from 0 to 400 nm using a 50 nm step, we sweep L_{s1} from 5 μm to 30 μm for each δw to find the combination of w_1, w_2, and L_{s1} that results in negligible ILs. For our purposes, we assumed ILs below 0.1 dB to be negligible. The simulated ILs as functions of L_{s1} for two sets of waveguide widths are shown in Fig. 3. Fig. 3(a) shows the results for S-bend waveguides with $w_1 = 550$ nm and $w_2 = 350$ nm, and Fig. 3(b) shows the results for S-bend waveguides with $w_1 = 600$ nm and $w_2 = 300$ nm. For the polarization independent coupler, we need to choose S-bend waveguides that have negligible ILs for both polarizations. By comparing the results shown in Fig. 3(a) and (b), we can see that

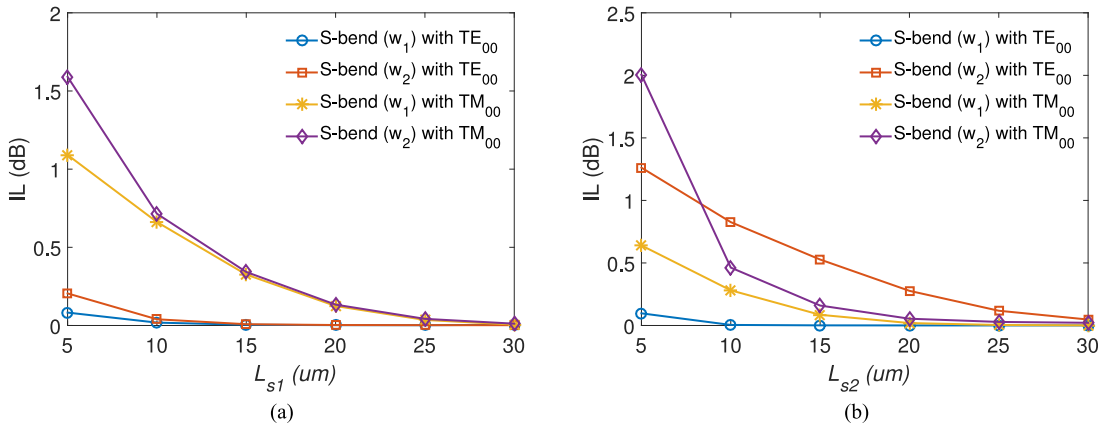

Fig. 3. Simulated ILs as functions of L_{S1} for injected TE_{00} and TM_{00} modes (a) with $w_1 = 550$ nm and $w_2 = 350$ nm and (b) with $w_1 = 600$ nm and $w_2 = 300$ nm.

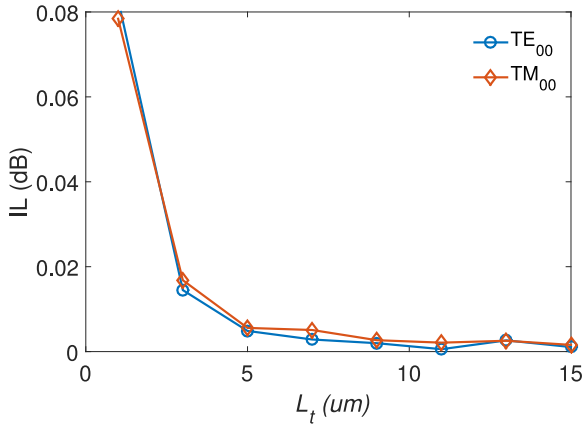

Fig. 4. Simulated ILs as functions of L_t for the taper that goes from width w to width w_2.

longer S-bend waveguides are required with $w_1 = 600$ nm and $w_2 = 300$ nm to achieve lower ILs. Therefore, we use $w_1 = 550$ nm, $w_2 = 350$ nm, and $L_{s1} = 30\,\mu$m for our coupler.

In the third step, we use 3D FDTD simulations to determine L_t. The length, L_t, is determined based on the ILs, and L_t needs to be long enough to allow adiabatic coupling of the optical modes from the left-hand side of Region I to the right-hand side of Region I. The simulated ILs as functions of L_t, for the TE_{00} and the TM_{00} modes of the bottom taper, from w to w_2, are shown in Fig. 4. Here, we assume that the ILs for the top taper, from w to w_1, will be lower since w_1 is greater than w_2. Based on the simulation results, we use $L_t = 10\,\mu$m for our coupler.

In the fourth step, we use the EME method to optimize Region III of our coupler and determined L. We inject the four lowest order modes of the two waveguide system, into the left-hand side of Region III, with $w_1 = 550$ nm and $w_2 = 350$ nm, and calculate the ILs of each of the injected mode on the right-hand side of Region III. The 1st order and the 2nd order modes of the two waveguide system are the excited modes when the TE_{00} mode is injected into Port1 or Port2, respectively, and the 3rd order and the 4th order modes of the two waveguide system are the excited modes when the TM_{00} mode is injected into Port1 or Port2, respectively. The simulated ILs as functions of L are shown in Fig. 5. It can be seen that evolutions of the TM modes occur over much shorter lengths than those of the TE modes, i.e., the TM mode require much smaller Ls. It should be noted that there is trade-off between the power imbalance and the design footprint of the coupler. Better power

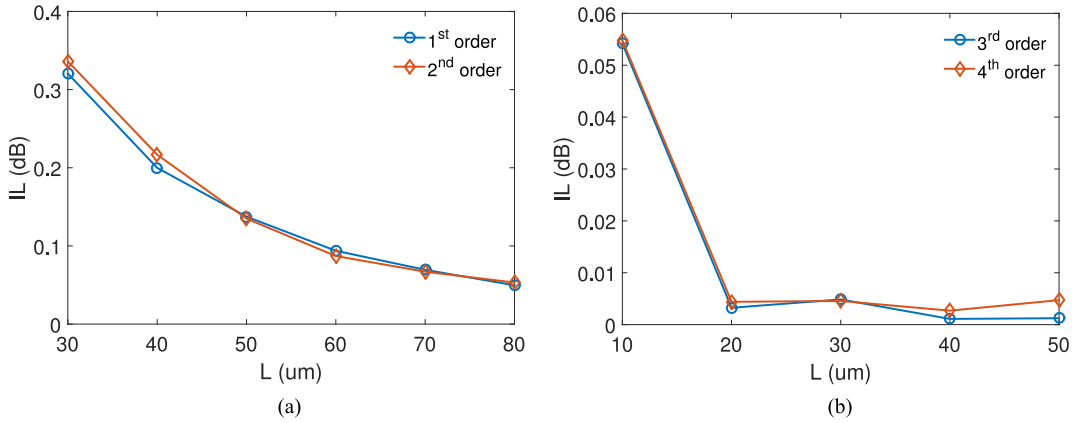

Fig. 5. Simulated ILs as functions of L, with $w_1 = 550$ nm and $w_2 = 350$ nm, for (a) the 1st order and the 2nd order modes, (b) the 3rd order and the 4th order mode.

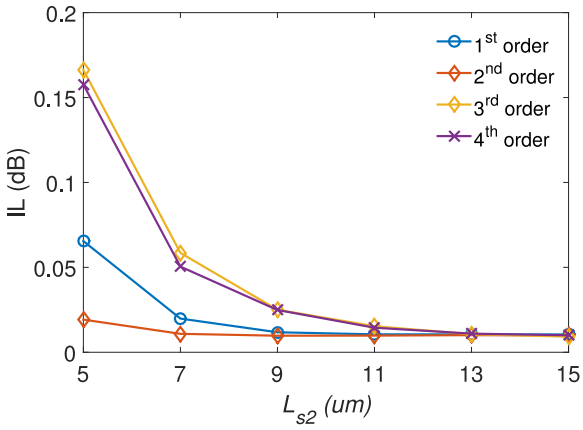

Fig. 6. Simulated ILs as functions of L_{s2} as functions of L_{s2}.

TABLE 1
Design Parameters of Our Polarization Independent Mode-Evolution-Based Coupler

g_1 (um)	w (nm)	w_1 (nm)	w_2 (nm)	L_t(um)	g_2 (nm)	L (um)	L_{s1}(um)	L_{s2}(um)
2.5	450	550	350	10	100	75	30	10

imbalance can be achieved at a cost of longer coupling length. In our case, we use $L = 75\,\mu$m for our coupler as a compromise between the power imbalance and design footprint.

In the fifth step, we use 3D FDTD simulations to optimize Region IV of our all couplers and determine L_{s2}. On the left-hand side of Region IV, either the 1st order or the 2nd order mode of the two waveguide system is excited when the TE_{00} mode is injected into either Port1 or Port2, respectively, and either the 3rd order or the 4th order mode of the two waveguide system is excited when the TM_{00} mode is injected into either Port1 or Port2, respectively. We measure the ILs of the S-bend waveguides using mode-expansion monitors on the right-hand side of Region IV for a particular mode. Based on the simulation results shown in Fig. 6, we use $L_{s2} = 10\,\mu$m for our coupler.

At this point, we have determined all the design parameters for our coupler, which are listed in Table 1.

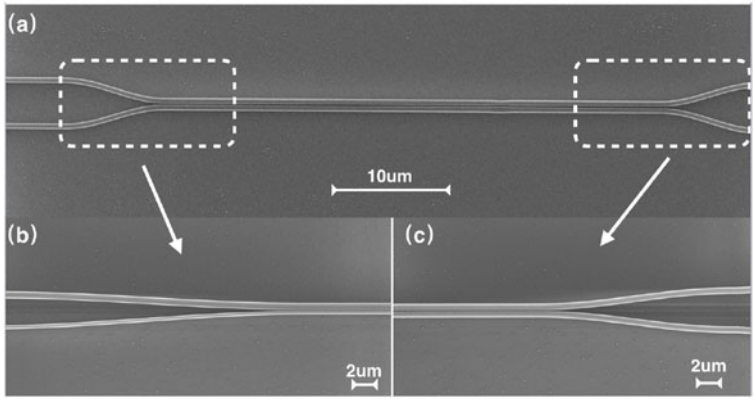

Fig. 7. (a) SEM image of a fabricated mode-evolution-based coupler, (b) zoom-in of the input S-bend waveguide region, and (c) zoom-in of the output S-bend waveguide region.

3. Fabrication and Experimental Results

Waveguide-based, unbalanced Mach-Zehnder interferometer (MZI) test structures, were used to characterize the power splitting ratios of our couplers. Such test structures have also been used to characterize other power splitters [6], [15]. Two identical couplers with mirror symmetry were used as the power splitter and the combiner for the MZI, and were connected by waveguides with a length difference of about 200 μm. The mismatch in the two arms of the MZI results in oscillations in the measured spectra, and the power splitting ratios of the couplers can be calculated using the wavelength dependent extinction ratios (ERs) extracted from the appropriate output spectrum. Test structures for our couplers were fabricated using electron beam lithography at Applied Nanotools Inc, using SOI wafers with a 220 nm silicon layer and a 2 μm buried oxide layer. A nominal 2.1 μm-thick silicon dioxide cladding layer was also used to protect the surface of the chip. Broadband sub-wavelength grating couplers were used to couple light into and out of the test structures [23]. Scanning electron microscope (SEM) images of a fabricated coupler are shown in Fig. 7. To make measurements using the fabricated test structures, a fiber array based test setup with a Yenista TUNICS T100S-HP C-band tunable laser and a CT400 passive optical component tester were used. The wavelength was swept from 1500 nm to 1600 nm using a 10pm step to obtain the spectra.

The power splitting ratios of the fabricated couplers can be calculated from their ERs using the measured spectra and the following equation [15]:

$$K = \frac{1}{2} \pm \frac{1}{2}\sqrt{\frac{1}{10^{\frac{ER}{10}}}} \tag{1}$$

where, ER denotes the ERs of the measured spectrum and K is the power coupling coefficient, i.e., the splitting ratios of the two couplers.

The measured spectra and calculated Ks for the polarization independent coupler are shown in Fig. 8. As the grating couplers are polarization sensitive, two test structures were used to characterize our polarization independent couplers. TE grating couplers were used as the inputs/outputs (Is/Os) of the first test structure, while TM grating couplers were used as the Is/Os of the second test structure. The polarization independent couplers used in the two test structures were the same and had mirror symmetry. Fig. 8(a) and (c) show the measured spectra for the polarization independent coupler for a TE_{00} mode and a TM_{00} mode, respectively, injected into the wider input waveguide of the first coupler of our MZI structure and measured from the wider output of the second coupler of the MZI structure. Fig. 8(b) and (d) show the calculated Ks as functions of wavelengths. The simulated Ks a functions of wavelengths using 3D FDTD simulations have also been shown in the graph for comparison purposes. As can be seen from Fig. 8, the fabricated polarization

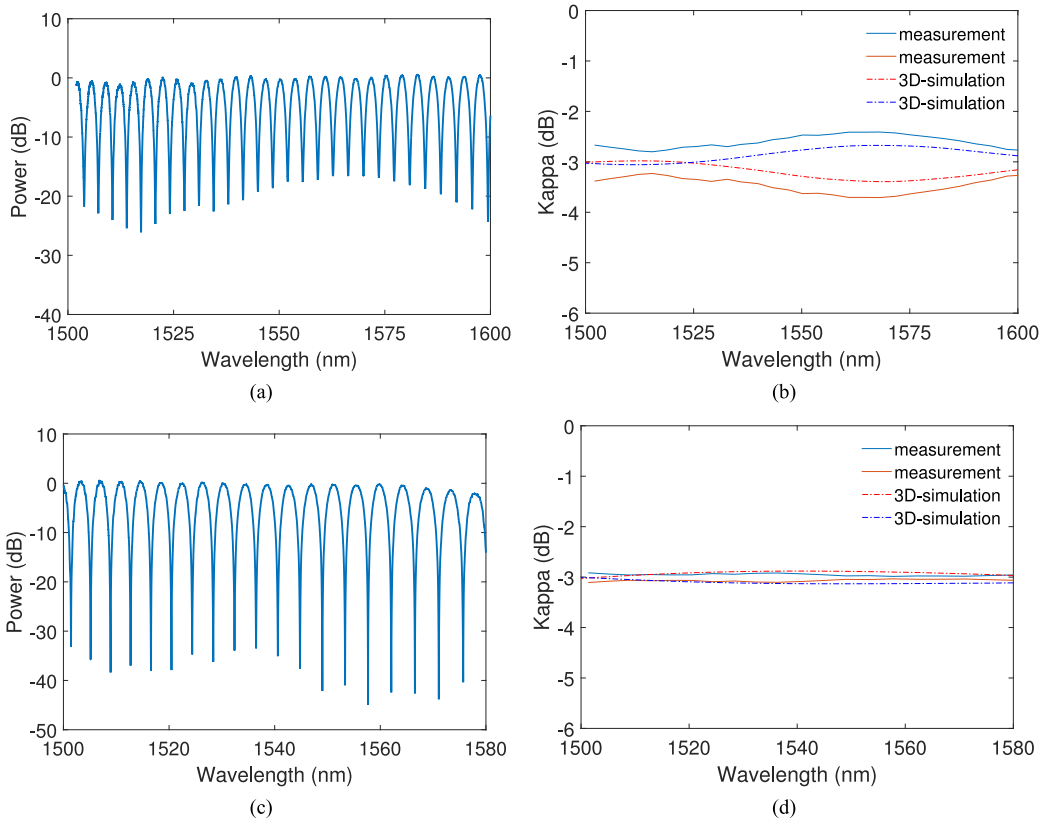

Fig. 8. (a) Measured spectra of the polarization independent coupler with TE input and (b) calculated and simulated power splitting ratios of the polarization independent coupler with TE input. (c) Measured spectra of the polarization independent coupler with TM input and (d) calculated and simulated power splitting ratios of the polarization independent coupler with TM input.

TABLE 2
Comparison of the State-of-the-Art Polarization Independent Couplers

Ref.	Power imbalance	Bandwidth	IL	Polarization dependent loss
[24]	negligible	45 nm	~ 0.2 dB	~ 0.4 dB
[25]	~ 3 dB	60 nm	< 1 dB	< 0.5 dB
[26]	~ 2 dB	80 nm	~ 1 dB	
This work	1.2 dB for TE, 0.2 dB for TM	100 nm	< 1 dB	~ 1 dB

independent coupler has a K of 3 ± 0.6 dB, i.e., a power imbalance of 1.2 dB, over the wavelength range from 1500 nm to 1600 nm for the TE_{00} mode and a K of 3 ± 0.1 dB, i.e., a power imbalance of 0.2 dB, over the wavelength range from 1500 nm to 1580 nm for the TM_{00} mode. The measured power imbalance agrees well with the simulation for the TM_{00} mode as shown in Fig. 8(d), while the measured power imbalance is slightly larger than the simulation for theTE_{00} mode as shown in Fig. 8(b). The increased power imbalance for the TE_{00} mode is resulted from the insufficient L of our coupler, which may caused by the enlarged g_2 during fabrication. The power imbalance for the TE_{00} mode is worse than the TM_{00} mode, which is also due to the insufficient length of the coupling region that we used for our coupler, and better power imbalance can be achieved for the TE_{00} mode with larger L values.

Mode-evolution-based polarization independent couplers have also been demonstrated recently [24]–[26]. The comparison between the state-of-the-art polarization independent couplers with the coupler demonstrated in this work are summarized in Table 2, where we can see that our coupler

has lower power imbalances and broader operating bandwidth. In addition, our coupler has better fabrication tolerance as compared to the mode-coupling-based couplers.

4. Conclusion

We have demonstrated a polarization independent mode-evolution-based 3-dB couplers for the SOI platform. The demonstrated coupler has negligible IL with operating bandwidth of about 100 nm. The measured maximum power imbalances of the polarization independent coupler are 1.2 dB and 0.2 dB for the TE_{00} mode and the TM_{00} mode, respectively. Compact design footprint, with a 75 μm long mode-evolution region is achieved. In addition, a segmented design approach based on a combination of the 3D FDTD and the EME methods has been presented. This approach significantly reduced the simulation time and computational demands of our design processes for the three couplers demonstrated in this paper. This design approach should be able to be used to reduce the simulation and design time of other computationally demanding mode-evolution-based devices.

References

[1] C. R. Doerr *et al.*, "Single-chip silicon photonics 100-Gb/s coherent transceiver," in *Proc. Opt. Fiber Commun. Conf. Exhib.*, 2014, Paper Th5C–1.

[2] P. Dong, X. Chen, K. Kim, S. Chandrasekhar, Y.-K. Chen, and J. H. Sinsky, "128-Gb/s 100-km transmission with direct detection using silicon photonic stokes vector receiver and I/Q modulator," *Opt. Express*, vol. 24, no. 13, pp. 14208–14214, 2016.

[3] M. R. Watts, J. Sun, C. DeRose, D. C. Trotter, R. W. Young, and G. N. Nielson, "Adiabatic thermo-optic Mach–Zehnder switch," *Opt. Lett.*, vol. 38, no. 5, pp. 733–735, 2013.

[4] M. A. Tran, C. Zhang, and J. E. Bowers, "A broadband optical switch based on adiabatic couplers," in *Proc. IEEE Photon. Conf.*, 2016, pp. 755–756.

[5] L. Cao, A. Elshaari, A. Aboketaf, and S. Preble, "Adiabatic couplers in SOI waveguides," in *Proc. Conf. Lasers Electro-Opt.*, 2010, Paper CThAA2.

[6] H. Yun, W. Shi, Y. Wang, L. Chrostowski, and N. A. F. Jaeger, "2 $\times$ 2 adiabatic 3-dB coupler on silicon-on-insulator rib waveguides," in *Proc. SPIE*, 2013, Paper 89150V.

[7] H. Yun, Z. Lu, Y. Wang, W. Shi, L. Chrostowski, and N. A. F. Jaeger, "2 $\times$ 2 broadband adiabatic 3-dB couplers on SOI strip waveguides for TE and TM modes," in *Proc. Conf. Lasers Electro-Opt.*, 2015, Paper STh1F–8.

[8] L. Xu *et al.*, "Polarization independent adiabatic 3-dB coupler for silicon-on-insulator," in *Proc. Conf. Lasers Electro-Opt.*, 2017, Paper SF1I–5.

[9] H. Yun, Y. Wang, F. Zhang, Z. Lu, S. Lin, L. Chrostowski, and N. A. F. Jaeger, "Broadband 2 $\times$ 2 adiabatic 3 dB coupler using silicon-on-insulator sub-wavelength grating waveguides," *Opt. Lett.*, vol. 41, no. 13, pp. 3041–3044, 2016.

[10] J. Xing, K. Xiong, H. Xu, Z. Li, X. Xiao, J. Yu, and Y. Yu, "Silicon-on-insulator-based adiabatic splitter with simultaneous tapering of velocity and coupling," *Opt. Lett.*, vol. 38, no. 13, pp. 2221–2223, 2013.

[11] A. Maese-Novo *et al.*, "Wavelength independent multimode interference coupler," *Opt. Express*, vol. 21, no. 6, pp. 7033–7040, 2013.

[12] P. Dumais *et al.*, "2 $\times$ 2 multimode interference coupler with low loss using 248 nm photolithography," in *Proc. Opt. Fiber Commun. Conf. Exhib.*, 2016, Paper W2A-19.

[13] J. N. Caspers and M. Mojahedi, "Measurement of a compact colorless 3 dB hybrid plasmonic directional coupler," *Opt. Lett.*, vol. 39, no. 11, pp. 3262–3265, 2014.

[14] Z. Lu *et al.*, "Broadband silicon photonic directional coupler using asymmetric-waveguide based phase control," *Opt. Express*, vol. 23, no. 3, pp. 3795–3808, 2015.

[15] Y. Wang *et al.*, "Compact broadband directional couplers using subwavelength gratings," *IEEE Photon. J.*, vol. 8, no. 3, Jun. 2016, Art. No. 7101408.

[16] M. Watts, H. Haus, and E. Ippen, "Integrated mode-evolution-based polarization splitter," *Opt. Lett.*, vol. 30, no. 9, pp. 967–969, 2005.

[17] M. Watts and H. Haus, "Integrated mode-evolution-based polarization rotators," *Opt. Lett.*, vol. 30, no. 2, pp. 138–140, 2005.

[18] W. D. Sacher, T. Barwicz, B. J. Taylor, and J. K. Poon, "Polarization rotator-splitters in standard active silicon photonics platforms," *Opt. Express* vol. 22, no. 4, pp. 3777–3786, 2014.

[19] Y. Shani, C. H. Henry, R. C. Kistler, R. F. Kazarinov, and K. J. Orlowsky, "Integrated optic mode-evolution-based devices on silicon," *IEEE J. Quantum Electron.*, vol. 27, no. 3, pp. 556–566, Mar. 1991.

[20] A. E.-J. Lim *et al.*, "Review of silicon photonics foundry efforts," *IEEE J. Sel. Topics Quantum Electron.*, vol. 20, no. 4, pp. 405–416, Aug. 2014.

[21] L. Chrostowski and M. Hochberg, *Silicon Photonics Design From Devices to Systems.* Cambridge, U.K.: Cambridge Univ. Press, 2015.

[22] S. K. Selvaraja *et al.*, "193 nm immersion lithography for high-performance silicon photonic circuits," in *Proc. SPIE*, vol. 9052, 2014, Paper 90520F.

[23] Y. Wang *et al.*, "Design of broadband subwavelength grating couplers with low back reflection," *Opt. Lett.*, vol. 40, no. 20, pp. 4647–4650, 2015.
[24] L. Liu, Q. Deng, and Z. Zhou, "Subwavelength-grating-assisted broadband polarization-independent directional coupler," *Opt. Lett.*, vol. 41, no. 7, pp. 1648–1651, 2016.
[25] X. Chen, W. Liu, Y. Zhang, and Y. Shi, "Polarization-insensitive broadband 2 $\times$ 2 3-dB power splitter based on silicon-bent directional couplers," *Opt. Lett.*, vol. 42, no. 19, pp. 3738–3740, 2017
[26] H. Xu and Y. Shi, "Ultra-compact polarization-independent directional couplers utilizing a subwavelength structure," *Opt. Lett.*, vol. 42, no. 24, pp. 5202–5205, 2017